Available online at www.sciencedirect.com
SCIENCE DIRECT®
Coordination Chemistry Reviews 248 (2004) 1317–1328
COORDINATION CHEMISTRY REVIEWS
www.elsevier.com/locate/ccr

Review

Stepwise assembly of amphiphilic ruthenium sensitizers and their applications in dye-sensitized solar cell

Md. K. Nazeeruddin [a,*], S.M. Zakeeruddin [a], J.-J. Lagref [a], P. Liska [a], P. Comte [a], C. Barolo [b], G. Viscardi [b], K. Schenk [c], M. Graetzel [a,*]

[a] *Laboratory for Photonics and Interfaces, Institute of Molecular and Biological Chemistry, School of Basic Sciences, Swiss Federal Institute of Technology, CH-1015 Lausanne, Switzerland*
[b] *Dipartimento di Chimica Generale ed Organica Applicata, Center for Nanostructured Surfaces and Interfaces, Università di Torino, Corso Massimo D'Azeglio 48, 10125 Torino, Italy*
[c] *Laboratory of Crystallography, University of Lausanne, Lausanne, Switzerland*

Received 16 October 2003; accepted 25 March 2004
Available online 13 May 2004

Contents

Abstract

A novel synthetic route for preparation of amphiphilic heteroleptic ruthenium(II) complexes of the type $[Ru(H_2dcbpy)Cl(cymene)]NO_3$ (**1**) $[Ru(H_2dcbpy)(dmbpy)(NCS)_2]$ (**2**), $[Ru(H_2dcbpy)(dhbpy)(NCS)_2]$ (**3**) $[Ru(H_2dcbpy)(dnbpy)(NCS)_2]$ (**4**) and $[Ru(H_2dcbpy)(dtdbpy)(NCS)_2]$ (**5**) have been developed starting from dichloro(*p*-cymene)ruthenium(II) dimer. The performance of these complexes as charge-transfer photosensitizers in nanocrystalline TiO_2-based solar cells was studied. When anchored complexes **2**–**5** onto a $12 + 4$ μm thick nanocrystalline

* Corresponding authors. Tel.: +41-216936124; fax: +41-216934111.
E-mail address: mdkhaja.nazeeruddin@epfl.ch (Md.K. Nazeeruddin).

doi:10.1016/j.ccr.2004.03.012

TiO_2 films achieve very efficient sensitization over 85 ± 5% incident photon-to-current efficiencies (IPCEs) in the visible region. Under standard AM 1.5 sunlight, using an electrolyte consisting of 0.6 M BMII; 0.05 M I_2; 0.1 M LiI; 0.5 M *tert*-butyl pyridine in 1:1 acetonitrile + valeronitrile the films yielded a short circuit photocurrent density of 16 ± 0.5 mA/cm^2 and the open circuit voltage was 700 ± 50 mV and a fill factor of 0.75 ± 0.05, corresponding to an overall conversion efficiency of 8.6%. Solar cells based on amphiphilic sensitizers show remarkable stability under both thermal stress and light soaking matching the durability criteria applied to silicon solar cells for outdoor applications.

Keywords: Amphiphilic heteroleptic ruthenium(II) sensitizers; Hydrophobic ruthenium complexes; Dye-sensitized solar cells; Photovoltaic cells; Nanocrystalline TiO_2 films; Solar energy conversion

1. Introduction

Dye-sensitized solar cells are currently attracting widespread academic and commercial interest for the conversion of sunlight into electricity because of their low cost and high efficiency. Over the past few years, considerable progress has been made in understanding the function of various components of dye-sensitized solar cells [1–20]. A schematic representation of operating principles and energy level diagram of dye-sensitized solar cell is shown in Fig. 1. In these cells, several ruthenium complexes containing anchoring groups such as carboxylic acid, dihydroxy, and phosphonic acid on pyridyl ligands have been used as dyes [21–23]. The anchoring groups serve to immobilize the dye on nanocrystalline TiO_2 surface. Photoexcitation of the metal-to-ligand charge transfer (MLCT) of the immobilized sensitizer (Eq. (1)), which leads to injection of electrons into the conduction band of the oxide (Eq. (2)). The oxidized dye is subsequently reduced by electron donation from an electrolyte containing the iodide/triiodide redox system (Eq. (3)). The injected electron flows through the semiconductor network to arrive at the back contact and then through the external load to the counter electrode. At the counter electrode, reduction of triiodide in turn regenerates iodide (Eq. (4)), through the donation of electrons from the external circuit, which completes the circuit. However, there are undesirable side reactions: the injected electrons may recombine either with oxidized sensitizer (Eq. (5)), or with the oxidized redox couple at the TiO_2 surface (Eq. (6)), resulting losses in the cell efficiency. For a net forward current under study state illumination, the processes of Eqs. (2) and (3) must be kinetically more favorable than those of Eqs. (5) and (6).

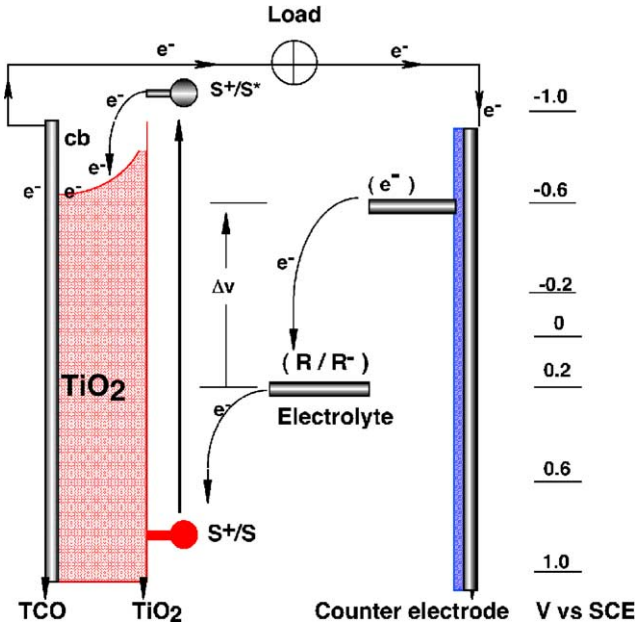

Fig. 1. Operating principles and energy level diagram of dye-sensitized solar cell. $S/S^+/S^*$: sensitizer in the ground, oxidized and excited state, respectively. R/R^-: redox mediator (I^-/I_3^-).

The overall conversion efficiency (η) of the dye-sensitized solar cell is determined by the photocurrent density (i_{ph}), the open circuit potential (V_{oc}), the fill factor (ff) of the cell and the intensity of the incident light (I_s) as shown in Eq. (7).

$$S\ (\text{adsorbed on } TiO_2) + h\nu \rightarrow S^*\ (\text{adsorbed on } TiO_2) \quad (1)$$

$$S^*\ (\text{adsorbed on } TiO_2) \rightarrow S^+\ (\text{adsorbed on } TiO_2) + e^-\ (\text{injected}) \quad (2)$$

$$S^+\ (\text{adsorbed on } TiO_2) + \tfrac{3}{2}I^- S\ (\text{adsorbed on } TiO_2) + \tfrac{1}{2}I_3^- \quad (3)$$

$$I_3^-\ (\text{cathode}) + 2e^- \rightarrow 3I^-\ (\text{cathode}) \quad (4)$$

$$S^+\ (\text{adsorbed on } TiO_2) + e^-\ (TiO_2) \rightarrow S\ (\text{adsorbed on } TiO_2) \quad (5)$$

$$I_3^- + 2e^-\ (TiO_2) \rightarrow 3I^-\ (\text{anode}) \quad (6)$$

$$\eta_{\text{global}} = i_{ph} V_{oc} \frac{ff}{I_s} \quad (7)$$

In these cells, the dye is one of the key components for high power conversion efficiencies. The optimal sensitizer for the dye-sensitized solar cell should fulfill several conditions: (i) it should harvest visible light of all colors and convert photons into electrons. (ii) It must be firmly grafted to the semiconductor oxide surface and inject electrons into the conduction band with a quantum yield of unity. (iii) To achieve high quantum yields of the excited state electron

transfer process, the dye ideally needs to be in intimate contact with the semiconductor surface and the excited state oxidation potential of the dye must energetically lie above the conduction band edge of the semiconductor. (iv) It should display directionality in the excited state. (v) Its ground state redox potential should be sufficiently high that it can be regenerated rapidly via electron donation from the electrolyte. (vi) It should be stable enough to sustain at least 10^8 redox turnovers under illumination corresponding to about 20 years of exposure to natural sunlight.

The pioneering studies on dye-sensitized solar cells using *cis*-dithiocyanatobis(4,4′-dicarboxylic acid-2,2′-bipyridine)-ruthenium(II) (N3) is a paradigm in this field [1,24]. A new development for dyes applied to solar cell comes from the preparation of amphiphilic heteroleptic N3-equivalents [25]. These amphiphilic heteroleptic sensitizers have several advantages compared to the N3 complex: (a) the ground state pK_a of the 4,4′-dicarboxy-2,2′-bpy in amphiphilic heteroleptic complex is higher compared to the N3 that enhances the binding of the complex onto the TiO_2 surface. (b) The presence of a hydrophobic moiety on the ligand in the amphiphilic heteroleptic complex increases the stability of solar cells towards water induced desorption. (c) The oxidation potential of amphiphilic heteroleptic complexes is cathodically shifted compared to the N3 sensitizer, which increases the reversibility of ruthenium III/II couple leading to enhanced stability. Nevertheless, the synthesis of such complexes in a reproducible way is a daunting task and indeed requires novel synthetic approaches.

Many groups including ours have reported the synthesis and characterization of heteroleptic complexes of ruthenium [Ru(L^1)(L^2)(L^3)] (where L = bidentate pyridyl ligands) starting from a polymeric $Ru(CO)_2Cl_2$ and $RuCl_2(dmso)_4$ complexes [26–28]. However, the disadvantages of these synthetic routes are non-reproducibility, low yields and a mixture of isomers. Here, we report a potential synthetic route for stepwise assembly of tailored ruthenium complexes of the type [Ru(H_2dcbpy)(dmbpy)$(NCS)_2$] (**2**), [Ru(H_2dcbpy)(dhbpy)$(NCS)_2$] (**3**) [Ru(H_2dcbpy)(dnbpy)$(NCS)_2$] (**4**) and [Ru(H_2dcbpy)(dtdbpy)$(NCS)_2$] (**5**) (Fig. 2) starting from dichloro(*p*-cymene)ruthenium(II) dimer and their application in dye-sensitized solar cells.

2. Experimental

2.1. Materials

The solvents (puriss grade, from Fluka), hydrated ruthenium trichloride (from Johnson Matthey), 4,4′-dimethyl-2,2′-bipyridine (dmbpy), 4,4′-dinonyl-2,2′-bipyridine (dnbpy), dichloro(*p*-cymene)ruthenium(II) dimer and potassium/ammonium thiocyanate were obtained (from Aldrich) and used as received. 4,4′-Dihexyl-2,2′-bipyridine and 4,4′-ditridecyl-2,2′-bipyridine were synthesized using literature procedures [25,29].

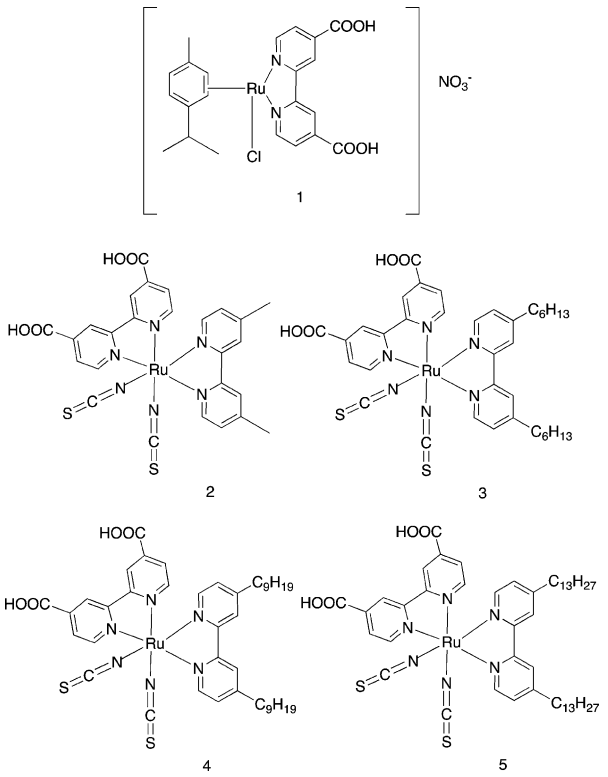

Fig. 2. Structures of the complexes **1**–**5**.

2.2. Analytical measurements

UV-Vis and fluorescence spectra were recorded in 1 cm path length quartz cell on a Cary 5 spectrophotometer and Spex Fluorolog 112 spectrofluorimeter, respectively. Electrochemical data were obtained by cyclic voltammetry in a conventional three-electrode cell with a PAR potentiostat. A glassy-carbon or a gold working electrode, platinum-wire auxiliary electrode and saturated silver chloride electrodes were used in a single-compartment-cell configuration. Proton and ^{13}C NMR spectra were measured on a Bruker 200 MHz spectrometer. The reported chemical shifts were in ppm against TMS. The FTIR spectra for all the samples were measured using a Digilab 7000 FTIR spectrometer. The ATR data reported here was taken with the 'Golden Gate' diamond anvil ATR accessory (Graseby-Specac) using typically 64 scans at a resolution of 2 cm^{-1}. The samples were all measured under the same mechanical force pushing the samples in contact with the diamond window. No ATR correction has been applied to the data. It also has to be appreciated that this ATR technique probes at most 1 μm of sample depth and that this depends on the sample refractive index, porosity, etc. The IR optical bench was flushed with dry air. The dye-coated TiO_2 films were rinsed in acetonitrile and dried at 150 °C before taking the spectra. The FTIR spectra of anchored dyes were obtained by subtracting the IR spectrum of the blank TiO_2 films from the IR spectrum of the dye coated TiO_2 films of the same thickness.

Table 1
Selected crystallographic data for [Ru(H_2dcbpy)Cl(cymene)]NO_3 (**1**)

Empirical formula	$[C_{22}H_{22}ClN_2O_4Ru]NO_3{\cdot}4H_2O$
Formula weight	649.01
Temperature (K)	125(2)
Wavelength (Å)	0.71073
Crystal system	Monoclinic
Space group	*I2/a*
Ru–N(1)	2.068(2)
Ru–N(2)	2.082(2)
Ru–C(14)	2.168(3)
Ru–C(18)	2.178(3)
Ru–C(15)	2.196(3)
Ru–C(17)	2.204(3)
Ru–C(13)	2.211(3)
Ru–C(16)	2.231(3)
Ru–Cl	2.3966(10)
N(1)–Ru–N(2)	77.22(9)
N(1)–Ru–C(14)	137.50(12)
N(2)–Ru–C(14)	92.11(10)
N(1)–Ru–C(18)	93.05(9)
N(2)–Ru–C(18)	137.62(11)
C(14)–Ru–C(18)	67.47(10)
N(1)–Ru–C(15)	172.35(10)
N(2)–Ru–C(15)	107.10(10)

2.3. Crystal diffraction study

Crystals of complex **1** were grown from slow evaporation of a methanolic solution containing complex **1**. The structure refinement results and the atomic coordinates are given in Table 1. The data collection for the plate-like single crystal 1 was performed at 210 K on an Enraf-Nonius CAD-4 diffractometer equipped with a graphite monochromator using Mo Kα radiation ($\lambda = 0.71073$ Å). A brown, irregular crystal of 1 was coated with a drop of Hostinter 216 and put into the orifice of a glass capillary. This was brought into a stream of nitrogen at $T = 125$ K on a Stoe IPDS system equipped with Mo radiation. The image plate–crystal distance was set to 70 mm and a ϕ interval of 1° was chosen. Two hundred images were then obtained during two minutes exposure. An inspection of reciprocal space revealed the crystal to be not of high quality. The structure was solved, with the help of DIRDIFand refined by means of SHELXTL [30]. All non-hydrogen atoms were refined anisotropically, the acid and water protons isotropically, but the other hydrogen atoms were made to ride on their associated carbons.

2.4. TiO_2 electrode preparation

TiO_2 anatase nanoparticles of 16 nm were prepared by hydrolysis of titanium(IV)isopropoxide as described before [31]. The nanocrystalline TiO_2 thin films of 12 μm thick were deposited onto transparent conducting glass (TEC-15, USA which has been coated with a fluorine-doped stannic oxide layer, sheet resistance of 12–15 Ω/cm^2) by screen printing. These films were dried at 150 °C for 20 min and then a 4 μm thick layer of 400 nm TiO_2 particles (400 nm particles were obtained from CCI, Japan) was deposited again using a screen printing method. The double layered films were sintered at 500 °C for 20 min.

The heated electrodes were impregnated with a 0.05 M titanium tetrachloride solution in a water saturated desiccator for 30 min at 70 °C and washed with distilled water. The 0.05 M titanium tetrachloride solution was prepared in the following manner: first, 2 M titanium tetrachloride solution was prepared by adding directly titanium tetrachloride liquid into a bottle containing ice, which was cooled to −20 °C, then the solution was further diluted to 0.05 M. Finally, the electrodes were heated at 520 °C for 20 min and allowed to cool to 50 °C before dipping into the dye solution.

Dye solutions were prepared in the concentration range of $2–3 \times 10^{-4}$ M in ethanol and the electrodes were dipped into the dye solution for 18–22 h. Alternatively, the heated TiO_2 electrodes were dipped for 20–30 min into a concentrated dye solution of 9×10^{-3} M in dimethylformamide (DMF) or a measured volume of 9×10^{-3} M solution in DMF was pipetted (10 μl for 0.5 cm^2 TiO_2 area) onto the surface of TiO_2 electrode and the dye solution left for 30 min [32]. The dye-coated electrodes were rinsed quickly with acetonitrile and used as such for photovoltaic measurements.

2.5. Dye-sensitized solar cell fabrication

The dye deposited film is used as a working electrode. A sandwich cell was prepared with a second conducting glass coated with chemically deposited platinum from 0.05 M hexachloroplatinic acid. The platinum coated counter electrode, and the dye coated TiO_2 film were then put together with a thin transparent film of Surlyn polymer frame (DuPont). The sandwiched electrodes were tightly held and then heat (130 °C) applied around the Surlyn frame to seal the two electrodes. A thin layer of electrolyte consisting of 0.6 M BMII; 0.05 M I_2; 0.1 M LiI; 0.5 M *tert*-butyl pyridine in 1:1 acetonitrile + valeronitrile was introduced into inter electrode space from the counter electrode side through pre-drilled holes. The drilled holes were sealed with microscope cover slide and Surlyn to avoid leakage of the electrolyte solution.

2.6. Photoelectrochemical measurements

Photoelectrochemical data were measured using a 450 W Xenon light source that was focused to give 1000 W/m^2, the equivalent of one sun at air mass 1.5, at the surface of the test cell. The spectral output of the lamp was matched in the region of 350–750 nm with the aid of a Schott KG-5 sunlight filter so as to reduce the mismatch between the simulated and the true Solar spectrum to less than 2%. The differing intensities were regulated with neutral wire mesh attenuators. The applied potential and measured cell current was measured using a Keithley model 2400 digital source meter. The current–voltage characteristics of the cell under these conditions were determined by biasing the cell externally and measuring the generated photocurrent. This

process was fully automated using Wavemetrics software. A similar data acquisition system was used to control the incident photon-to-current conversion efficiency (IPCE) measurement. Under full computer control, light from a 300 W Xe lamp was focused through a high throughput monochromator onto the photovoltaic cell under test. The monochromator was incremented through the visible spectrum to generate the IPCE (λ) curve as defined below

$$\mathrm{IPCE}(\lambda) = 1240\left(\frac{I_{sc}}{\lambda\phi}\right)$$

where λ is the wavelength, I_{sc} the current at short circuit (mA/cm^2), and ϕ the incident radiative flux (W/m^2). The photoelectrochemical properties were investigated by measuring the current and voltage (*I–V*) characteristics.

3. Synthesis and characterization

*3.1. Synthesis of [Ru(H_2dcbpy)Cl(cymene)]NO_3 (**1**) (H_2dcbpy= 4,4′-dicarboxy-2,2′-bipyridine)*

4,4′-Dicarboxy-2,2′-bipyridine (0.078 g, 0.32 mmol) ligand was dissolved in 30 ml DMF in presence of two equivalents of tetrabutyl ammonium hydroxide solution in water (0.1 ml). To this solution was added [RuCl(*p*-cymene)]$_2$ (0.1 g, 0.16 mmol) as a solid. The reaction mixture was heated at 60 °C, under nitrogen for 4 h. After allowing it to cool to room temperature, it was filtered through sintered (G-4) glass crucible and then the filtrate was evaporated completely. The resulting solid was dissolved in water and precipitated by adding 0.01 M HNO_3. The orange-yellow solid was filtered and dried under vacuum. Yield 0.139 g, 75%. The precipitated solid was re-crystallized from methanol and diethyl ether.^{1}H NMR (CD_3OD, δ ppm, *J* Hz): 9.49 (2H, d, $H^{6,6'}$, *J* 5.8); 8.89 (2H, d, $H^{3,3'}$, *J* 1.5); 8.11 (2H, d, $H^{5,5'}$, *J* 5.8); 6.15 (*p*-cymene, 2H, d, *J* 6.5); 5.90 (*p*-cymene, 2H, d, *J* 6.5); 3.70 (*p*-cymene, H, q, CH); 2.31 (s, *p*-cymene, CH3); 1.09 (d, *p*-cymene, CH(C(CH3)$_2$, *J* 6.92), Analysis found: C, 46.21%; H, 4.19%; N, 7.19%. Calculated: C, 46.66%; H, 4.26%; N, 7.10% for $C_{23}H_{25}ClN_3O_7Ru$.

*3.2. Synthesis of [Ru(H_2dcbpy)(dmbpy)(NCS)$_2$] (**2**) (H_2dcbpy = 4,4′-dicarboxy-2,2′-bipyridine, dmbpy = 4,4′-dimethyl-2,2′-bipyridine)*

In a typical synthesis, [$RuCl_2$(*p*-cymene)]$_2$ (0.1 g, 0.16 mmol) was dissolved in DMF (50 ml) to which was added 4,4′-dimethyl-2,2′-bipyridine (0.058 g, 0.32 mmol) as a solid. The reaction mixture was heated to 55–65 °C under nitrogen for 4 h with constant stirring. After this period, H_2dcbpy (0.08 g, 0.32 mmol) was added as a solid and refluxed at 155–165 °C for 4 h. Then, excess of NH_4NCS (0.76 g, 10 mmol) was added to the reaction mixture and continued refluxing for another 5 h at 140–150 °C. The reaction flask was allowed to cool to 25 °C and the solution was filtered through a G4 sintered glass crucible. The solvent was removed by using a rotary-evaporator under vacuum. The resulting solid was washed with water to remove excess of NH_4NCS and the insoluble product was collected on a sintered glass crucible by suction filtration. The solid was further washed with distilled water and diethyl ether. The crude complex was purified on a Sephadex LH-20 column using methanol as an eluent.

The complex **2** was also obtained by reacting equal molar ration of complex **1** with 4,4′-dimethyl-2,2′-bipyridine ligand, followed by excess of NH_4NCS in DMF under nitrogen.

^{1}H NMR (δ_H (ppm) in CD_3OD) 9.66 (d, 1H), 9.27 (d, 1H), 9.05 (s, 1H), 8.90 (s, 1H), 8.5 (s, 1H), 8.34 (s, 1H), 8.32 (d, 1H), 7.88 (d, 1H), 7.70 (d, 2H), 7.65 (d, 1H), 7.37 (d, 1H) 7.05 (d, 1H), 2.91 (s, 3H), 2.45 (s, 3H).

Analysis found: C, 47.23%; H, 3.33%; N, 12.59%. Calculated: C, 47.05%; H, 3.34%; N, 12.66% for $C_{26}H_{20}N_6O_4RuS_2\cdot H_2O$.

*3.3. Synthesis of [Ru(H_2dcbpy)(dhbpy)(NCS)$_2$] (**3**) (H_2dcbpy = 4,4′-dicarboxy-2,2′-bipyridine, dhbpy = 4,4′-dihexyl-2,2′-bipyridine)*

Using the same conditions as for complex **2**, starting from ligand 4,4′-dihexyl-2,2′-bipyridine the title compound was obtained as a dark powder. Yield 65%.

^{1}H NMR (δ_H (ppm) in CD_3OD) 9.66 (d, 1H), 9.26 (d, 1H), 9.02 (s, 1H), 8.87 (s, 1H), 8.51 (s, 1H), 8.37 (s, 1H), 8.18 (d, 1H), 7.85 (d, 1H), 7.67 (d, 2H), 7.61 (d, 1H), 7.39 (d, 1H) 7.05, 3.15 (t), 2.7(t), 1.95 (m), 1.57 (m), 1.0 (t).

Analysis found: C, 54.90%; H, 5.17%; N, 10.61%. Calculated: C, 55.01%; H, 5.13%; N, 10.6% for $RuC_{36}H_{40}N_6O_4S_2$.

*3.4. Synthesis of [Ru(H_2dcbpy)(dnbpy)(NCS)$_2$] (**4**) (H_2dcbpy = 4,4′-dicarboxy-2,2′-bipyridine, dnbpy = 4,4′-dinonyl-2,2′-bipyridine)*

Using the same conditions as for complex **2**, starting from ligand 4,4′-dinonyl-2,2′-bipyridine the title compound was obtained as a dark powder. Yield 60%.

^{1}H NMR (δ_H (ppm) in CD_3OD) 9.72 (d, 1H), 9.28 (d, 1H), 9.08 (s, 1H), 8.92 (s, 1H), 8.55 (s, 1H), 8.42 (s, 1H), 8.28 (d, 1H), 7.88 (d, 1H), 7.70 (t, 2H), 7.40 (d, 1H), 7.05 (d, 1H), 2.95 (t, 2H), 2.75 (t, 2H), 1.95 (m, 2H), 1.40 (m, 26H), 0.90 (t, 6H).

Analysis found: C, 57.90%; H, 5.97%; N, 9.61%. Calculated: C, 57.99%; H, 5.98%; N, 9.66% for $RuC_{42}H_{52}N_6O_4S_2$.

*3.5. Synthesis of [Ru(H_2dcbpy)(tdbpy)(NCS)$_2$] (**5**) (H_2dcbpy = 4,4′-dicarboxy-2,2′-bipyridine, tdbpy = 4,4′-tridecyl-2,2′-bipyridine)*

Using the same conditions as for complex **2**, starting from ligand 4,4′-tridecyl-2,2′-bipyridine the title compound was obtained. Yield, 60%.

^{1}H NMR (δ_H (ppm) in CD_3OD) 9.70 (d, 1H), 9.3 (d, 1H), 9.1 (s, 1H), 8.95 (s, 1H), 8.55 (s, 1H), 8.40 (s, 1H), 8.28 (d, 1H), 7.95 (d, 1H), 7.70 (d, 2H), 7.65 (d, 1H), 7.41 (d, 1H) 7.15, 3.15 (t), 2.7 (t), 1.9 (m), 1.45 (m), 0.98 (t).

Analysis found: C, 60.95%; H, 7.08%; N, 8.45%. Calculated: C, 61.13%; H, 6.98%; N, 8.56% for $RuC_{50}H_{68}N_6O_4S_2$.

4. Results and discussion

4.1. Synthetic studies

Scheme 1 shows the details of the synthetic strategy adopted for the preparation of heteroleptic complexes. During the reaction, aliquots of the intermediate products were withdrawn and characterized by NMR and UV-Vis spectra. Reaction of dichloro(*p*-cymene)ruthenium(II) dimer in *N*,*N*′-dimethylformamide (DMF) solution at 60 °C with 4,4′-substituted-2,2′-bipyridine (L) ligand resulted in a

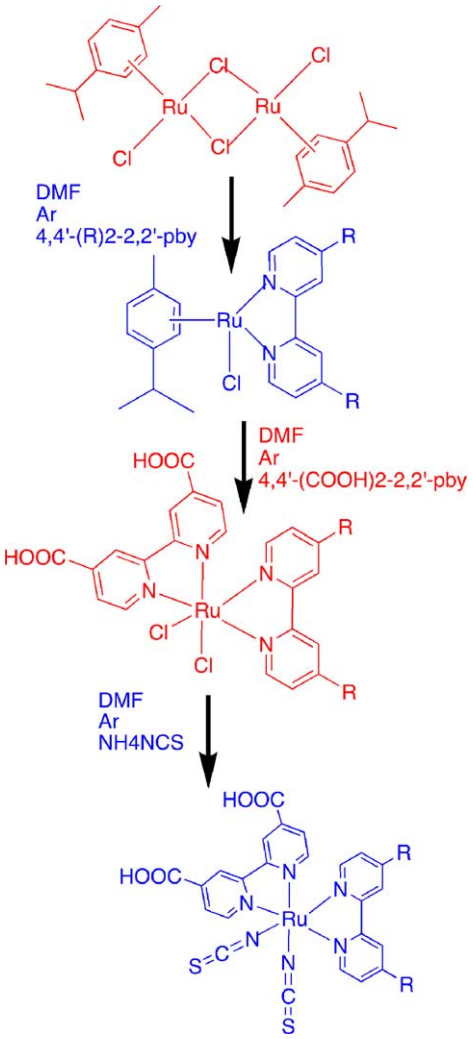

Scheme 1. The synthetic strategy adopted for the preparation of *cis*-amphiphilic heteroleptic complexes.

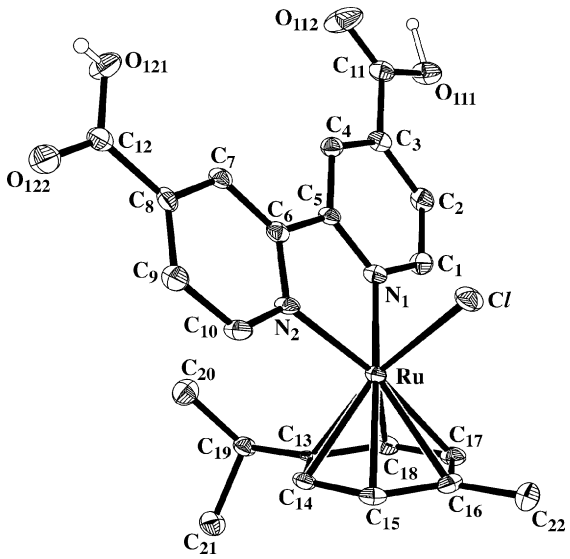

Fig. 3. Projection of molecular structure of **1** on the plane shows the symmetrical orientation of 4,4′-dicarboxy-2,2′-bipyridine ligand in relation to the cymene cycle.

mononuclear complex. In this step, coordination of substituted bipyridine ligand to the ruthenium center takes place with cleavage of the doubly chloride-bridged structure of the dimeric complex [33]. The proton NMR spectra of the mononuclear complex show three pyridine protons (two doublets and one singlet) and two cymene protons (two doublets) in the aromatic region. The presence of three protons clearly indicates that the bipyridine ligand is *trans* to the cymene group, which is consistent with the solid state crystal structure of the complex **1** (Fig. 3).

The heteroleptic dichloro complexes were prepared by reacting the mononuclear [Ru(4,4′-disubstituted-2,2′-bpy)Cl(cymene)]Cl complex with the H_2dcbpy ligand in DMF under reduced light at 150 °C. The UV-Vis spectral properties of $[Ru(L)(L')(Cl)_2]$ (L = 4,4′-dicarboxy-2,2′-bipyridine, L′ = 4,4′-dialkyl-2,2′-bipyridine) complexes are identical to the same complexes prepared by using the $RuCl_2(DMSO)_4$ method [25]. The chloride ligand, which is out side the coordination sphere in the complex **1** is pushed back into the coordination sphere even in presence of a coordinating solvent DMF. Displacement of the cymene ligand from the coordination sphere of ruthenium metal by substituted bipyridine ligand takes place efficiently in organic solvents (ethanol and DMF) even under dark at 100 °C. However, when the reaction was carried out in ethanol, formation of ≈15% *trans* isomer is evident. Therefore, it is necessary to use high boiling solvents to reflux the reaction mixture at 150 °C in order to obtain the more thermodynamically stable *cis* geometrical isomer.

The $[Ru(L)(L')(Cl)_2]$ complex was reacted with 30-fold excess of ammonium thiocyanate ligand to obtain the $[Ru(L)(L')(NCS)_2]$ complex. The NMR of the crude complex shows presence of 95% N-bonded and 5% S-bonded

isomers, which were separated on a Sephadex, LH-20 column of 2 cm × 30 cm, using methanol as an eluent.

4.2. Description of the structure of $[Ru(H_2dcbpy)Cl(cymene)]NO_3$

Selected crystal data, relevant bond distances and torsion angles of the complex **1** are given in Table 1. The geometry of crystal **1** was observed to be similar to the other structurally characterized ruthenium complexes [34]. The solid state structure of complex **1** is consistent with NMR data for the sample in solution. The structure of the cation shown in Fig. 3 consists of a ruthenium(II) atom coordinated to a chloride, a η^6-cymene and a 4,4′-dicarboxy-2,2′-bipyridine ligands. The Ru–N distances, 2.068 (Ru–N(1)) and 2.082 (Ru–N2) Å, are somewhat shorter when compared to related structures that contains 2,2′-bipyridine (Ru–N(1) = 2.08, Ru–N(2) = 2.084) and 1,10-phenanthroline (Ru–N(1) = 2.090, Ru–N(2) = 2.084) [35]. The observed shorter interatomic distances of complex **1** compared to 2,2′-bipyridine and 1,10-phenanthroline complexes, could be due to increased back bonding from the metal t_{2g} orbital to the π^* orbital of the 4,4′-dicarboxy-2,2′-bipyridine ligand compared to the analogous 2,2′-bipyridine. Consequently, the inter atomic distance of Ru–Cl is slightly longer in complex **1** compared to the analogous 2,2′-bipyridine complex.

4.3. NMR spectral data

The NMR spectrum of complex **1** displays two doublets and a singlet at δ 9.49; 8.89 and 8.11 ppm due to H6, H3 and H5 protons, respectively. The cymene aromatic protons are observed as two doublets at δ 6.15 and 5.90 ppm. The proton NMR spectrum of the first step of complex **2** shows a similar pattern however, the proton resonance signals were observed at a significantly higher field compared to the complex **1**, which can be explained in terms of the acceptor properties of the 4,4′-dicarboxy-2,2′-bipyridine compared to the 4,4′-dimethyl-2,2′-bipyridine.

Proton NMR spectra of the intermediate dichloro heteroleptic complex $[Ru(L)(L')(Cl)_2]$ (L = 4,4′-dicarboxy-2,2′-bipyridine, L′ = 4,4′-dialkyl-2,2′-bipyridine) is complicated in DMSO-d_6 solvent because of the labile nature of the chloride ligands. Nevertheless, in CD_3OD solvent, the chloride ligands seems to be stable and the proton NMR spectra of the dichloro heteroleptic complexes show the expected peaks, which are down field shifted compared to the *cis*-dithiocyanate complexes **2**–**5**.

The symmetry in heteroleptic complexes of type **2**–**5** is lowered when compared to the corresponding homoleptic complexes. Hence, the NMR spectra of these complexes are expected to be much more complicated. In these complexes, the two halves of each ligand is necessarily in different magnetic environment. Fig. 4 shows a representative proton NMR spectra of complex **2**, which show 12 resonance peaks in the aromatic region and two methyl resonance peaks in the aliphatic region corresponding to two different methyl groups of 4,4′-dimethyl-2,2′-bipyridine. The coordination induced chemical shifts of methyl protons of 4,4′-dimethyl-2,2′-bipyridine were attributed to the donor nature of the ligand. The apparent difference in the 4 and 4′ methyl protons is due to the *trans* effect.

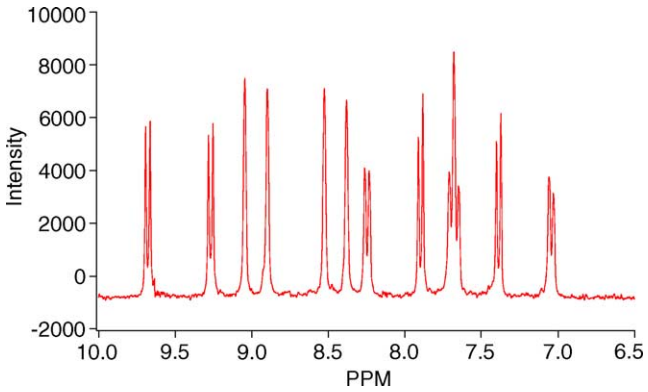

Fig. 4. Proton NMR spectrum of complex **2** in CD_3OD.

Carbon 13 NMR spectra of complexes **2**–**5**, were useful to identify the mode of coordination of thiocyanate ligand. The *N*-coordinated thiocyanate carbon resonance peak has been reported in a number of complexes at 130–135 ppm [36]. In complexes **2**–**5**, the two peaks at 136–133 ppm are due to the *N*-coordinated thiocyanate ligand, which are *trans* to the carboxylic acid pyridine and alkyl substituted pyridine, respectively. In the aromatic region (δ 170–120 ppm), complexes **2**–**5** show 22 resonance signals corresponding to 22 carbons of two different bipyridyl ligands. The peaks between δ 10–50 ppm, are due to the aliphatic resonance carbon signals. A representative ^{13}C NMR spectrum of complex **2** is shown in Fig. 5.

4.4. ATR-FTIR spectral data

ATR-FTIR spectra of the complexes **2**–**5** measured as a solid samples show a strong broad band in the region of at 1700 cm^{-1} due to carboxylic acid groups. The intense peak in the region of 1230 cm^{-1} is due to υ(C–O) stretch [37]. The band due to υ(NC) of the thiocyanate ligand was observed in the range of 2100–2115 cm^{-1} in complexes, **2**–**5**. ATR-FTIR spectra of the complexes **2**–**5** adsorbed on TiO_2 film show the presence of carboxylate asymmetric 1593 cm^{-1} $\upsilon(-COO_{as}{}^-)$ and symmetric 1383 cm^{-1} $\upsilon(-COO_s{}^-)$ bands together with a strong υ(NC) of the thiocyanate group at 2103 cm^{-1}. The presence of carboxylate bands in the IR spectra of adsorbed complexes of **2**–**5** on TiO_2 indicate that the two carboxylic acid groups are dissociated and involved in the adsorption on the TiO_2 surface.

4.5. Electronic spectra

The complexes **2**–**5** show broad and intense visible bands between 390 and 540 nm region due to metal-to-ligand

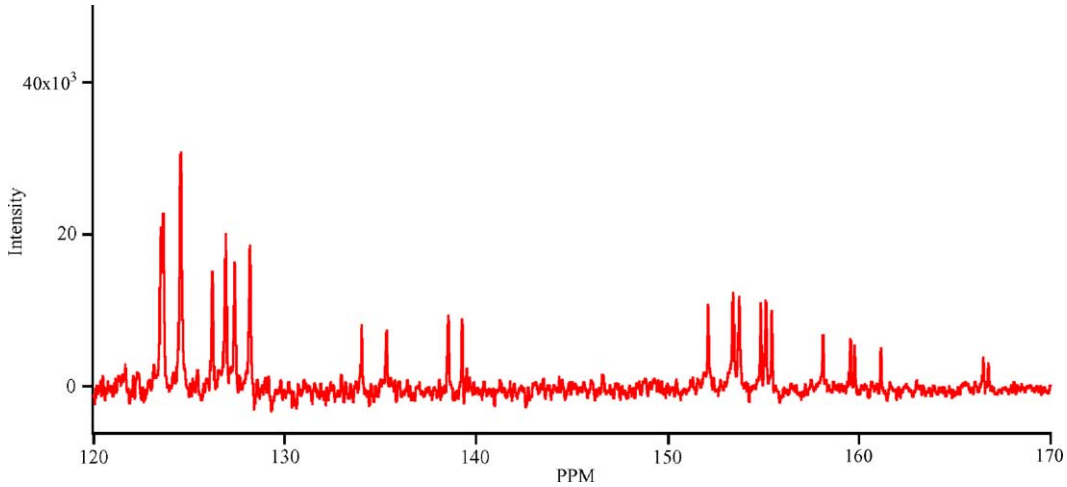

Fig. 5. ^{13}C NMR spectrum of the complex **2** measured in CD_3OD solvent.

charge-transfer transitions [38]. The complex **2** in dry ethanol shows two broad visible bands at 524 and 383 nm that are assigned to metal-to-ligand charge-transfer (MLCT) origin. The bands in the UV region at 295 and 312 nm are assigned to intra ligand (π–π^*) charge-transfer transitions of dmbpy and dcbpy ligands, respectively [39]. The lowest MLCT band of complex **2**, in ethanol lies at 524 nm, which is blue shifted (from 539 to 524 nm) compared to the homoleptic complex *cis*-dithiocyanatobis(4,4′-dicarboxylic acid-2,2′-bipyridine)ruthenium(II) that show a maximum at 539 nm. However, when compared to the dmbpy homoleptic complex (*cis*-dithiocyanatobis(4,4′-dimethyl-2,2′-bipyridine)ruthenium(II)), which show a maximum at 512 nm, the lowest MLCT band of complex **2**, is red shifted (from 512 to 524 nm), due to the electron withdrawing nature of the COOH groups at the 4,4′-positions of the bipyridine ligand, which lowers the energy of π^* orbital of the ligand compared to that of dmbpy.

Deprotonation of the COOH groups in complex **2** blue shifts the π–π^* charge-transfer band from 312 to 310 nm and the low energy MLCT band from 524 to 514 nm (Fig. 6). The blue shift is due to an increase in the energy of the LUMO of the ligand, causing the π–π^* and dπ–π^* transitions to occur at higher energies. However, the band at 294 nm due to dmbpy π–π^* charge-transfer transitions, is unaffected in the pH range 2–12. In complexes **2**–**5**, the molar extinction coefficient of the π–π^* charge-transfer transitions of 4,4′-dialkyl-2,2′-bipyridine is 35–40% higher than compared to the molar extinction coefficient of 4,4′-dicarboxy-2,2′-bipyridine π–π^* charge-transfer transitions. There are also two shoulders at 360 and 500 nm, which are tentatively attributed to a metal-to-ligand charge-transfer transitions involving the dmbpy ligand. The UV-Vis spectral properties of the complexes **3**–**5** are very similar to the complex **2**. The molar extinction coefficient of the lowest energy MLCT band in heteroleptic complexes **2**–**5** is 25% lower compared to the *cis*-dithiocyanatobis(4,4′-dicarboxylic acid-2,2′-bipyridine)ruthenium(II) complex. For comparison, the UV-Vis spectral data of homoleptic complex of *cis*-dithiocyanatobis(4,4′-dicarboxylic acid-2,2′-bipyridine)ruthenium(II) complex, were included in Table 2.

The absorption spectra of the complexes **2**–**5** anchored on 6 μm thick TiO_2 nanocrystalline electrode show the low energy MLCT maximum at 528 nm, which is considerably

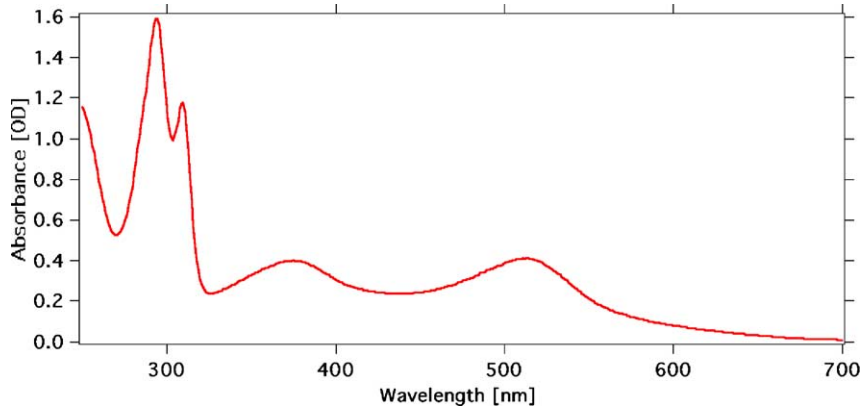

Fig. 6. UV-Vis absorption spectrum of the deprotonated complex **2**. The concentration of the solution was 3.5×10^{-5} M in ethanol.

Table 2
Absorption, photophysical and electrochemical properties of the ruthenium complexes

Complex	Absorption maximum[a] (nm) (ε ($10^4\,M^{-1}\,cm^{-1}$))			Emission[b] λ_{max}	τ[c] (ns)	$E_{1/2}$[d] Ox (ΔE (V))	$E_{1/2}$[d] Red (ΔE (V))
	π–π^*L^1	π–π^*L^2	dπ–π^*			$Ru^{III/II}$	4,4′-dcbpy
2	295 (4.54)	312 (3.35)	383 (1.13) 524 (1.16)	750	37	0.78 (0.08)	−1.5 (0.09)
3	296 (4.26)	312 (3.20)	384 (1.01) 525 (1.11)	760	29	0.73 (0.1)	−1.57 (0.07)
4	295 (4.24)	312 (3.01)	385 (1.09) 526 (1.16)	769	27	0.74 (0.08)	−1.62 (0.07)
5	296 (4.21)	312 (3.02)	384 (1.08) 525 (1.15)	760	29	0.74 (0.08)	−1.60 (0.07)
N3		314 (4.82)	398 (1.4) 539 (1.42)	830	20	0.85	–

[a] The data are referred to the protonated complexes measured in ethanol. L^1 and L^2 represent 4,4′-dialkyl-2,2′-bpy and 4,4′-dcbpy, respectively.
[b] Emission data were obtained by exciting at lowest energy MLCT band at 530 nm, without degassing at room temperature. The recorded values ±2 nm.
[c] Measured in ethyl alcohol at room temperature.
[d] The electrochemical data were measured in DMF solvent with 0.1 M tetrabutyl ammonium hexafluorophosphate using a gold (or glassy carbon) electrode. The reported data are V vs. SCE.

red shifted compared to the solution spectra of deprotonated complex in ethanol. This is due to the fact that on the electrode the carboxylate groups bind to the TiO_2 surface in which Ti^{4+}acts as an electron acceptor similar to proton causing slight decrease the LUMO of dcbpy. The lowest energy MLCT band maximum of the protonated state complex in solution is similar to that of the same complex adsorbed onto the TiO_2 surface. The complexes **2**–**5** adsorbed onto the TiO_2 surface is slightly higher in quantity compared to the standard N3 dye. The amount of dye adsorbed on the 6 μm thick TiO_2 nanocrystalline electrode from dilute solutions of 3×10^{-4} M in 1:1 acetonitrile and *tert*-butanol over 24 h is comparable to the dye adsorbed from 9×10^{-3} M solution in DMF over 30 min.

4.6. Emission spectra

Emission data of complexes **2**–**5** were obtained for air saturated solutions at room temperature by exciting at 530 nm in ethanol solution. The emission maxima of theses complexes in deprotonated state is at a higher energy and is more intense when compared with those observed from the protonated form. Emission lifetime data are consistent with the trend observed in emission intensities. The red-shifted emission from the protonated form of the complexes is due to stronger p-acceptor properties of the COOH group lowering the energy of the CT excited state. The π^* orbital of the protonated ligand is lower in energy than that of the deprotonated form. The shorter-lived emission lifetime in the acid form of the complexes is due to proton-induced quenching of the excited state [40].

4.7. Electrochemical data

Electrochemical data for complexes **2**–**5** measured using a gold or a glassy carbon electrode in DMF solvent with 0.1 M tetrabutyl ammonium hexafluorophosphate are compiled in Table 2. As observed, the complexes **2**–**5** displayed one ruthenium-centered oxidation and two ligand-based reduction couples between +1 to −1.9 V versus, SCE. Fig. 7 shows a typical cyclic voltammogram of the complex **4**, measured using a gold electrode with a scan rate of 1000 mV/s. Upon scanning to positive potentials, a quasi reversible couple at $E_{1/2} = 0.74$ V versus SCE with a separation of 0.08 V between anodic to cathodic peak was observed due to the $Ru^{II/III}$ couple (Fig. 7, process *B*). The couple at $E_{1/2} = 0.46$ V versus SCE labeled as A is due to ferrocenium/ferrocene couple, which was used as an internal standard. The ruthenium oxidation potential in complex **4** is shifted negatively by 0.11 V, compared to the *cis*-dithiocyanatobis(4,4′-dicarboxylic acid-2,2′-bipyridine)ruthenium(II) couple. The difference (0.11 V) in the oxidation potential of complex **4** compared to the N3 complex is due to presence of 4,4′-nonyl-2,2′-bpy in 4, which is a stronger donor compared to the 4,4′-dicarboxylic acid-2,2′-bipyridine.

The complex **4**, when scanning towards negative potentials with 1000 mV/s exhibited an irreversible wave and two quasi-reversible waves. The irreversible wave at −1.24 V is due to reduction of carboxylic acid protons to hydrogen. Wolfbauer et al. [41], have observed a similar behavior, deprotonation followed by

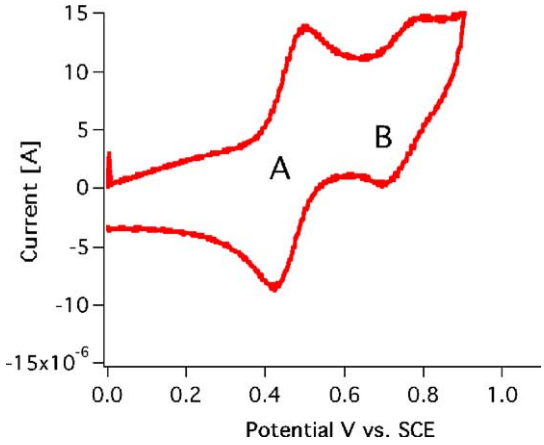

Fig. 7. Cyclic voltammogram of complex **4** measured in DMF solution containing 0.1 M TBA(PF_6) using a gold electrode with scan speed of 1000 mV/s. The couple labeled as A at $E_{1/2} = 0.46$ V vs., SCE is due to ferrocenium/ferrocene, which was used as an internal standard. The couple labeled as B at $E_{1/2} = 0.74$ V vs., SCE is due to the $Ru^{III/II}$.

reduction of the protons of the $dcbpyH_2$ ligand in $[Ru(dcbpyH_2)_2(NCS)_2]$ complex at a platinum electrode. However, on a glassy carbon electrode this process is absent. Based on the electrochemical properties of the homoleptic complexes of *cis*-dithiocyanatobis(4,4′-dicarboxylic acid-2,2′-bipyridine)ruthenium(II) and *cis*-dithiocyanatobis(4,4′-dimethyl-2,2′-bipyridine)ruthenium(II), the two quasi-reversible waves at $E_{1/2} = -1.62$ V and $E_{1/2} = -1.88$ V versus, SCE are assigned to the reduction of dcbpy and dmbpy ligand, respectively. The separation between the anodic and the cathodic peaks of the first reduction couple is 0.07 V, and the second couple is 0.11 V.

4.8. Photovoltaic performance

The TiO_2 electrodes were heated at 400 °C for 20 min before dipping them into the dye solution. The electrodes were left for 18–22 h in dilute solution of 3×10^{-4} M in ethanol or 1:1 acetonitrile + *tert*-butanol. Alternatively, a measured volume of the concentrated solution 9×10^{-3} M in DMF was pipetted (10 μl for 0.5 cm^2 TiO_2 area) onto the surface of the TiO_2 electrode and the dye solution left for 10–30 min. The dye-coated electrodes were rinsed quickly with acetonitrile and used as such for photovoltaic measurements. The photovoltaic performance of cells dipped between for 30 min in concentrated solution and 18 h in dilute solution are similar.

The performance of **2**–**5** as sensitizers on nanocrystalline TiO_2 electrode were studied using an electrolyte having composition of 0.6 M *N*-methyl-*N*-butyl imidazolium iodide, 0.05 M iodine, 0.05 M LiI and 0.5 M *tert*-butylpyridine in a 50:50 (v/v) mixture of valeronitirile and acetonitrile. The photocurrent action spectra obtained with the TiO_2 films coated with a monolayer of complex **5** in a sandwich cell under illumination by simulated AM 1.5 solar light is shown in Fig. 8. The incident monochromatic photon-to-current conversion efficiency (IPCE) is plotted as a function of excitation wavelength showing a plateau region at 90%. The photocurrent action spectra of the amphiphilic heteroleptic complexes show broad features covering a large part of the visible spectrum. From the overlap integral of this curve with the standard global AM 1.5 solar emission spectra one measures a short circuit photocurrent density of 16.5 mA/cm^2. In agreement with this, measurement under standard global AM 1.5 solar conditions the cell gave a photocurrent density of 16.2 mA/cm^2, 740 mV open circuit potential and 0.72 fill factor yielding close to 8.6% efficiency.

The current–voltage characteristics of a sandwich-type cell with 12 + 4 μm thick TiO_2 films sensitized by complexes **2**–**5** are shown Fig. 9. Under identical conditions, the short circuit photocurrent density of dyes **2**–**5**, slightly increases with increasing chain length. The photo voltage of the cell containing the complex **2** is lower than the complexes **3**–**5**. Very similar data were obtained for TiO_2 electrodes, which were dipped for 30 min in dye solutions of 9×10^{-3} M in DMF. The important effect asserted by the 4 μm thick 400 nm particles layer is evident in the red region of the IPCE curve. The incident monochromatic photon-to-current conversion efficiency at 700 nm is twice as high for the TiO_2 film containing a scattering layer as compared to the 7 μm thick TiO_2 film without a scattering layer.

4.9. Photovoltaic stability

The dye-sensitized solar cells so far have been plagued by performance degradation at temperatures between 80 and 85 °C [42,43]. The stability of solar cells with the amphiphilic ruthenium complexes in conjunction with the polymer gel and liquid electrolyte were investigated. Particularly, using the complex **4** several nanocrystalline solar cells were fabricated and subjected both to thermal stress and light soaking. The stability data of the complex **4** show remarkably stable performance [2]. The power conversion efficiency of the cell was sustained 94% of its initial value under heating for 1000 h at 80 °C. The tolerance to such

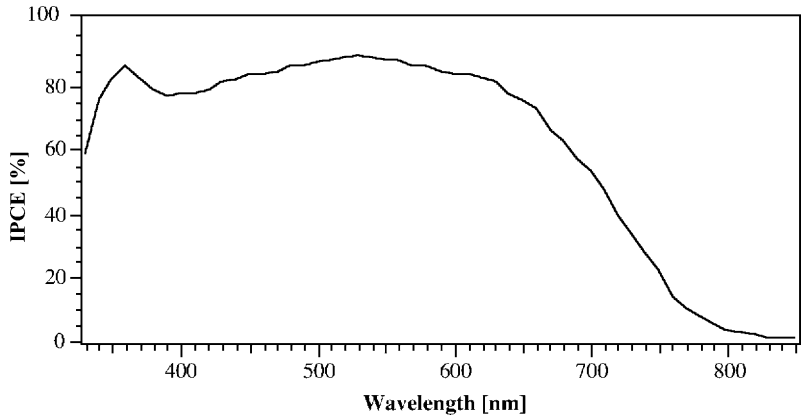

Fig. 8. Photocurrent action spectrum obtained with the complex **5** attached to nanocrystalline TiO_2 film. The incident photon to current conversion efficiency is plotted as a function of the wavelength of the exciting light. The electrolyte composition was 0.6 M *N*-methyl-*N*-butyl imidazolium iodide, 0.05 M iodine, 0.05 M LiI and 0.5 M *tert*-butylpyridine in a 50:50 (v/v) mixture of valeronitrile and acetonitrile.

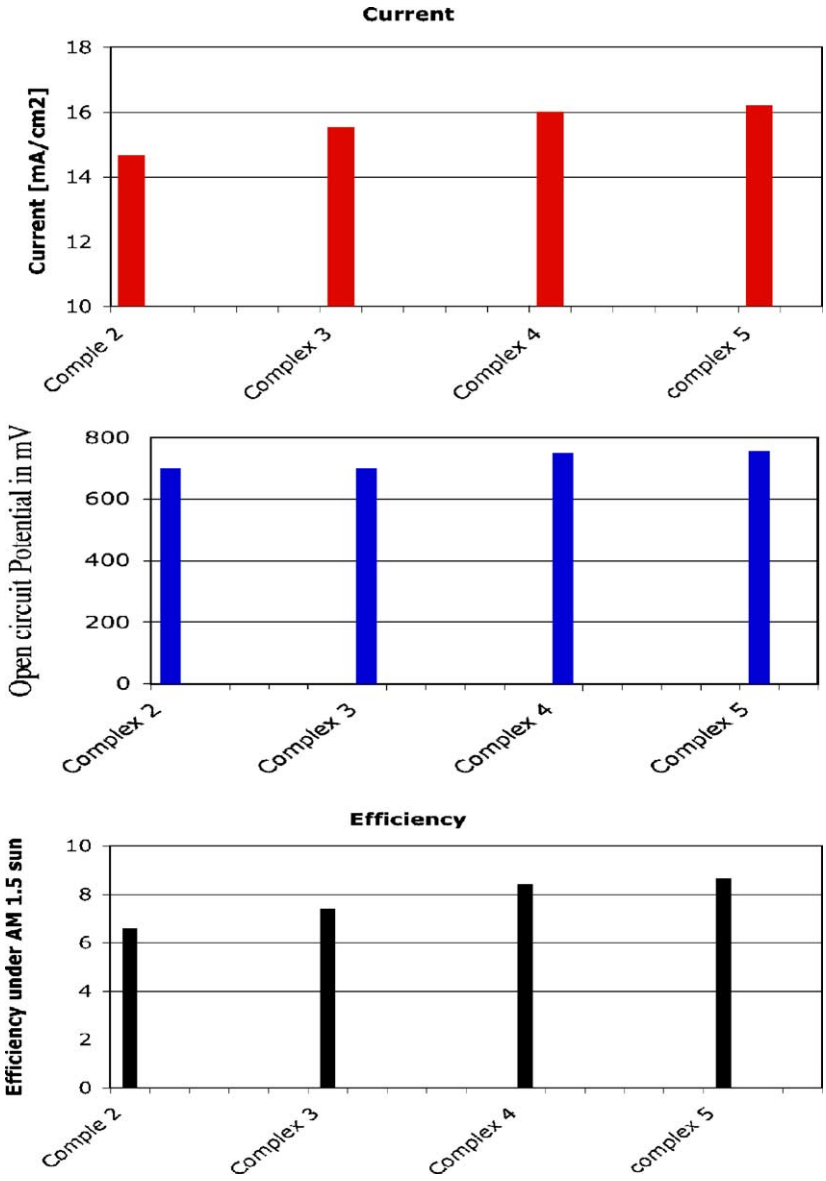

Fig. 9. Comparison of photocurrent (top chart), open circuit potential (middle chart) and the efficiency (bottom chart) obtained using complexes **2**–**5** on $12 + 4\,\mu m$ thick TiO_2 electrodes under AM 1.5 sun. The composition of the electrolyte used in these measurements is 0.6 M *N*-methyl-*N*-butyl imidazolium iodide, 0.05 M iodine, 0.05 M LiI and 0.5 M *tert*-butylpyridine in a 50:50 (v/v) mixture of valeronitirile and acetonitrile.

severe thermal stress and light soaking for nanocrystalline TiO_2-based dye-sensitized solar cells having less than a 10% decrease in efficiency from the initial value, is unprecedented.

Our observations reveal that by engineering dyes at the molecular level and fine-tuning their ground and excited state properties one could overcome the myth of stability problems associated with nanocrystalline TiO_2 dye-sensitized solar cells. Thus, this class of amphiphilic sensitizers serves as the basis for the design of new supramolecular sensitizers containing pyridyl ligands substituted with amide groups, which exhibit hydrogen bonding and organic lipid layers. These supramolecular sensitizers are expected to reduce the back electron transfer to the oxidized redox couple and thereby should benefit the open circuit potential resulting increase in overall efficiency of the solar cells. We are currently addressing the research directed towards this goal in our laboratory.

5. Conclusions

In the present study, we have identified the dimeric $[Ru(Cl)_2(cymene)]_2$ complex as a very convenient precursor to synthesize, amphiphilic heteroleptic complexes. It has been demonstrated that the cleavage of the dimer during the addition of a bidentate ligand affords a mononuclear $[Ru(H_2dcbpy)Cl(cymene)]$ (**1**) complex and further

the displacement of the cymene ligand from the coordination sphere of ruthenium metal by substituted bipyridine ligand takes place efficiently. This new simple and reproducible synthetic route can be an efficient way to synthesize amphiphilic heteroleptic complexes containing different functionalized ligands. The photovoltaic data of these new complexes show 8.6% power conversion efficiency under AM 1.5 sun, and unprecedented stability under thermal stress and light soaking. We have demonstrated that by engineering dyes at the molecular level and fine-tuning their ground and excited state properties one could overcome the saga of stability problems associated with nanocrystalline TiO_2 dye-sensitized solar cells.

Acknowledgements

We acknowledge financial support of this work by the Swiss Federal Office for Energy (OFEN), US Air Force Research Office under contract number F61775-00-C0003, and NANOMAX (contract No. ENK6-CT-2001-00575 of the 5th RTD framework program by EU and funded by OFES, Bern). We thank Dr. N. Vlachopoulos and D. Di Censo for their assistance in electrochemical measurement and Dr. Robin Humphry-Baker for his time and helpful discussions.

References

[1] M.K. Nazeeruddin, A. Kay, I. Rodicio, R. Humphry-Baker, E. Muller, P. Liska, N. Vlachopoulos, M. Grätzel, J. Am. Chem. Soc. 115 (1993) 6382.
[2] P. Wang, S.M. Zakeeruddin, J.E. Moser, M.K. Nazeeruddin, T. Sekiguchi, M. Graetzel, Nat. Mater. 2 (2003) 402.
[3] R.D. McConnell, Renewable Sustainable Energy Rev. 6 (2002) 273.
[4] K.D. Benkstein, N. Kopidakis, J. van de Lagemaat, A.J. Frank, J. Phys. Chem. B 107 (2003) 7759.
[5] K. Hara, T. Sato, R. Katoh, A. Furube, Y. Ohga, A. Shinpo, S. Suga, K. Sayama, H. Sugihara, H. Arakawa, J. Phys. Chem. B 107 (2003) 597.
[6] S. Nakade, Y. Saito, W. Kubo, T. Kitamura, Y. Wada, S. Yanagida, J. Phys. Chem. B 107 (2003) 8607.
[7] Y. Tachibana, S.A. Haque, I.P. Mercer, J.E. Moser, D.R. Klug, J.R. Durrant, J. Phys. Chem. B 105 (2001) 7424.
[8] J.E. Moser, D. Noukakis, U. Bach, Y. Tacchibana, D.R. Klug, J.R. Durrant, R. Humphry-Baker, M. Grätzel, J. Phys. Chem. B 102 (1998) 3649.
[9] G. Boschloo, H. Lindstrom, E. Magnusson, A. Holmberg, A. Hagfeldt, Photochem. Photobiol. A Chem. 148 (2002) 11.
[10] S. Ferrere, B.A. Gregg, J. Phys. Chem. B 105 (2001) 7602.
[11] C.A. Bignozzi, R. Aragazzi, C.J. Kleverlaan, Chem. Soc. Rev. 29 (2000) 87.
[12] J.B. Asbury, N.A. Anderson, E. Hao, X. Ai, T. Lian, J. Phys. Chem. B 107 (2003) 7376.
[13] G. Oskam, B.V. Bergeron, G.J. Meyer, P.C. Searson, J. Phys. Chem. B 105 (2001) 6867–6873.
[14] G. Sauvé, M.E. Cass, S.J. Doig, I. Lauermann, K. Pomykal, N.S. Lewis, J. Phys. Chem. 104 (2000) 3488.
[15] M.-A. De Paoli, D.A. Machado, A.F. Nogueira, C. Longo, Electrochim. Acta 46 (2001) 4243.
[16] Y.-J. Hou, P.-H. Xie, B.-W.Z. Jing, Y. Cao, X.-R. Xiao, W.-B. Wang, Inorg. Chem. 38 (1999) 6320.
[17] G.R.A. Kumara, A. Konno, K. Shiratsuchi, J. Tsukahara, K. Tennakone, Chem. Mater. 14 (2002) 954.
[18] B. Lemon, J.T. Hupp, J. Phys. Chem. B. 103 (1999) 3797.
[19] S. Sakaki, T. Kuroki, T. Hamada, J. Chem. Soc., Dalton Trans. (2002) 840.
[20] S.G. Chen, S. Chappel, Y. Diamant, A. Zaban, Chem. Mater. 13 (2001) 4629.
[21] P.-H. Xie, Y.J. Hou, B.W. Zhang, Y. Cao, F. Wu, W.-J. Tian, J.C. Shen, J. Chem. Soc., Dalton Trans. (1999) 4217.
[22] M.K. Nazeeruddin, S.M. Zakeeruddin, R. Humphry-Baker, T.A. Kaden, M. Grätzel, Inorg. Chem. 39 (2000) 4542.
[23] C.R. Rice, M.D. Ward, M.K. Nazeeruddin, M. Grätzel, New J. Chem. 24 (2000) 651.
[24] M.K. Nazeeruddin, S.M. Zakeeruddin, R. Humphry-Baker, M. Jirousek, P. Liska, N. Vlachopoulos, V. Shklover, C.H. Fischer, M. Grätzel, Inorg. Chem. 38 (1999) 6298.
[25] S.M. Zakeeruddin, M.K. Nazeeruddin, R. Humphry-Baker, P. Pechy, P. Quagliotto, C. Barolo, G. Viscardi, M. Graetzel, Langmuir 18 (2002) 952.
[26] P.A. Anderson, G.F. Strouse, J.A. Treadway, F.R. Keene, T.J. Meyer, Inorg. Chem. 33 (1994) 3863.
[27] J.M. Clear, J.M. Kelly, C.M. O'Connell, J.G. Vos, C.J. Cardin, S.R. Costa, A.J. Edwards, J. Chem. Soc., Chem. Commun. (1980) 750.
[28] D.S.C. Black, G.B. Deacon, N.C. Thomas, Inorg. Chim. Acta 65 (1982) L75.
[29] D.K. Ellison, R.T. Iwamoto, Tetrahedron Lett. 24 (1983) 317.
[30] G.M. Sheldrick, SHELXTL 5.05 ed., Bruker Analytical X-Ray Instruments Inc., Madison, WI, 1996.
[31] M.K. Nazeeruddin, P. Pe'chy, T. Renouard, S.M. Zakeeruddin, R. Humphry-Baker, P. Comte, P. Liska, C. Le, E. Costa, V. Shklover, L. Spiccia, G.B. Deacon, C.A. Bignozzi, M. Gra1tzel, J. Am. Chem. Soc. 123 (2001) 1613.
[32] M.K. Nazeeruddin, R. Splivallo, P. Liska, P. Comte, M. Grätzel, Chem. Commun. (2003) 1456.
[33] S.B. Wendicke, E. Burri, R. Scopelliti, K. Severin, Organometallics 22 (2003) 1894.
[34] M.T. Ashby, S.S. Alguindigue, M.A. Khan, Organometallics 19 (2000) 547.
[35] C. Menéndez, D. Morales, J. Pérez, V. Riera, Organometallics 20 (2001) 2775.
[36] M.K. Nazeeruddin, S.M. Zakeeruddin, R. Humphry-Baker, S.I. Gorelsky, A.B.P. Lever, M. Grätzel, Coord. Chem. Rev. 208 (2000) 213.
[37] A. Fillinger, B.A. Parkinson, J. Electrochem. Soc. 146 (1999) 4559.
[38] V. Balzani, A. Juris, M. Venturi, S. Campagna, S. Serroni, Chem. Rev. 96 (1996) 759.
[39] T.J. Meyer, Pure Appl. Chem. 50 (1986) 1293.
[40] K. Kalyanasundaram, M.K. Nazeeruddin, Chem. Phys. Lett. 193 (1992) 292.
[41] G. Wolfbauer, A.M. Bond, G.B. Deacon, D.R. MacFarlane, L. Spiccia, J. Am. Chem. Soc. 122 (2000) 130.
[42] H. Pettersson, T. Gruszecki, L.H. Johansson, P. Johander, Sol. Energy Mater. 77 (2003) 405.
[43] B. Macht, M. Turrion, A. Barkschat, P. Salvador, K. Ellmer, H. Tributsch, Sol. Energy Mater. 73 (2002) 163.